Check for updates

Small

NANO · MICRO small
www.small-journal.com

RESEARCH ARTICLE OPEN ACCESS

Micro-Corrugated Hydrogel Electrodes for High-Performance Biofuel Cells via Capillary Force and Ligand Exchange-Induced Metal Nanoparticle Assembly

Eunju Choi[1] | Jun Hyung Kim[1] | Su Hwan Kim[1] | Hye Min Yu[1] | Gee Chan Jin[1] | Jeongmin Mo[2] | Junha Pak[2] | Seung-Kyum Choi[3] | Jongkuk Ko[4] | Jinhan Cho[2,5] | Cheong Hoon Kwon[1]

[1]Department of Energy Resources and Chemical Engineering, Kangwon National University, Samcheok, Republic of Korea | [2]Department of Chemical & Biological Engineering, Korea University, Seoul, Republic of Korea | [3]GeorgeW. Woodruff School of Mechanical Engineering, Georgia Institute of Technology, Atlanta, Georgia, USA | [4]School of Chemical, Biological, and Battery Engineering, Gachon University, Seongnam si, Gyeonggi-do, Republic of Korea | [5]KU-KIST Graduate School of Converging Science and Technology, Korea University, Seongbuk-gu, Seoul, Republic of Korea

Correspondence: Jongkuk Ko (kojk@gachon.ac.kr) | Jinhan Cho (jinhan71@korea.ac.kr) | Cheong Hoon Kwon (chkwon2@kangwon.ac.kr)

Received: 11 October 2025 | **Revised:** 1 December 2025 | **Accepted:** 15 December 2025

Keywords: complementary interaction mediated assembly | conductive hydrogel | enzyme-based biofuel cells | micro-corrugated structure

ABSTRACT

Biocompatible enzyme-based biofuel cells (EBFCs) with enzymatic electrodes show great potential as power sources for wearable and implantable biomedical devices. However, their practical application has been limited by poor electron transfer efficiency and insufficient operational stability. In this study, we present a mediator-free, hydrogel-based EBFC that addresses these challenges through the integration of capillary force-assisted assembly and hydrophobic metal nanoparticle (NP) deposition. The resulting highly conductive hydrogel electrode enables enhanced power output and long-term stability. To achieve this goal, the hydrogel, composed of poly(ethylene imine) functionalized with amine ($-NH_2$) groups, was immersed in a solution of tetra(octylammonium) (TOA)-stabilized Au NPs. This process induced ligand exchange reaction and room-temperature NP fusion at the interface between the NH_2-functionalized hydrogel and the hydrophobic Au NPs, along with capillary-force-driven self-assembly, thereby converting the initially insulating hydrogel into a highly conductive hydrogel with micro-corrugated structure. Subsequently, glucose oxidase and TOA-Au NPs were deposited onto the conductive, micro-corrugated hydrogel to construct the anode, while a platinum (Pt)-modified hydrogel served as the cathode. This EBFC achieved a high-power output of ~3.7 mW cm^{-2} and maintained ~80% of initial power after 30 days of continuous operation, representing a significant advancement toward hydrogel-based EBFC.

1 | Introduction

The rapid growth of various portable and medical electronic devices, including microscale systems and implantable systems, has intensified the demand for energy sources, underscoring the need for renewable and sustainable energy solutions [1–6]. Among the emerging candidates, enzyme-based biofuel cells (EBFCs) have garnered considerable attention due to their environmentally friendly and renewable nature. In particular, EBFCs can efficiently generate electricity from biofuels, such as glucose and oxygen, under physiological conditions, making them an attractive power source for implantable medical devices [3, 4, 7–10]. Despite these advantages, however, the practical deployment of EBFCs remains limited by

Eunju Choi and Jun Hyung Kim contributed equally to this work.

This is an open access article under the terms of the Creative Commons Attribution-NonCommercial-NoDerivs License, which permits use and distribution in any medium, provided the original work is properly cited, the use is non-commercial and no modifications or adaptations are made.
© 2025 The Author(s). *Small* published by Wiley-VCH GmbH

their inherently low power output and insufficient operational stability [3, 11, 12].

To address these challenges, various strategies have been explored, primarily aimed at enhancing electron transfer at the host electrode/enzyme and enzyme/enzyme interfaces to boost power output, as well as optimizing enzyme immobilization to improve the operational stability. Additionally, significant progress has been made in developing soft, biocompatible host electrodes with high electrical conductivity as alternatives to conventional carbon-based electrodes, which often suffer from lower conductivity compared to bulk metal-based materials [13–15]. Achieving high electrical conductivity in the host electrode is crucial for efficient electron transfer between electrode and enzymes.

Although mediated electron transfer (MET)-based EBFCs are capable of achieving relatively high power densities (e.g., 2.18 mW cm^{-2}), their reliance on diffusible mediators introduces drawbacks—including mediator leakage and reduced open-circuit voltage (OCV)—that limit their suitability for in vivo use [16]. By contrast, mediator-free EBFCs inherently offer superior biocompatibility and improved long-term stability, motivating increasing efforts to advance their development for wearable and implantable bioelectronic platforms [17, 18].

A widely adopted strategy to enhance electron transfer involves the incorporation of conductive fillers, such as carbon nanotubes (CNTs) and metal nanoparticles (NPs), into enzyme layers [19–22]. For example, glucose oxidase (GOx)—commonly used in EBFC anodes—has its redox active site (flavin adenine dinucleotide, FAD) buried 7–15 Å beneath an insulating protein surface, which limits electron transfer to the host electrode as well as between adjacent GOx molecules [21]. For addressing this limitation, the incorporated conductive fillers act as electron relays, facilitating electron transfer and thereby enhancing overall power output. Nevertheless, even with such fillers, the achieved power densities often remained insufficient [23, 24]. More recently, a few studies have reported mediator-free EBFCs achieving unprecedented power outputs of several mW cm^{-2}, sparking growing interest in the development of mediator-free systems [8].

In addition to enhancing the power output of electron relay-based EBFCs, improving enzyme immobilization remains a critical challenge [9, 25, 26]. Although various immobilization strategies—such as weak adsorption (via van der Waals forces and hydrogen bonding), covalent bonding, cross-linking, and physical entrapment—have been explored, they are still prone to enzyme leaching, particularly due to their dependence on slurry casting, which often overlooks interfacial interaction at the electrode/enzyme and enzyme/enzyme interfaces [27–29]. Therefore, a key challenge is to devise a strategy that can simultaneously promote efficient electron transfer for high power output and ensure stable enzyme immobilization. Securely anchoring the enzymes not only prevents leaching but also enhances electron transfer efficiency by maintaining close contact between the enzymes and adjacent conductive components.

Furthermore, the choice of host electrode is also important in the design of biocompatible and soft EBFCs. Among various candidates, hydrogels are widely recognized as highly biocompatible materials that are generally safe for use in living systems. To transform these intrinsically insulating hydrogels into electrically conductive hydrogels, various conductive fillers—such as CNTs [30], metal components [31–35], and conductive polymers [36–40]—are incorporated into the hydrogel matrix via solution blending [41], following a similar strategy to that used for enhancing electron relay effects in enzyme-based systems. However, most conductive hydrogels still exhibit relatively low conductivity, typically in the range of ~10^{-5} to 10^{1} S cm^{-1}. This limitation primarily arises from high contact resistance between adjacent conductive fillers or from the inherently low conductivity of certain fillers, such as carbon-based materials—even when used at high loading levels. Therefore, achieving an electrically stable hydrogel host electrode with exceptionally high electrical conductivity (exceeding 10^{4} S cm^{-1}) remains a significant challenge, particularly when conductive components are directly deposited onto the surface of wet and insulating hydrogels through complementary interfacial interaction, rather than incorporated via simple solution blending or slurry casting. Although interfacial printing, hot pressing, and interfacial metal-assembly approaches (e.g., galvanic replacement, electroless deposition, and in situ metal-ion reduction) have been explored to create conductive metallic structures, these methods often provide limited control over NP organization and exhibit weak adhesion to soft, water-rich hydrogel interfaces [42–45]. Similarly, previously reported soft electrode (i.e., elastomer-based electrode) typically rely on bulk mixing or surface-coating strategies that offer poor nanostructural controllability and inadequate anchoring sites for enzymes, rendering them unsuitable for high-performance EBFC electrodes [46]. More critically, these approaches fail to provide stable enzyme immobilization—an essential requirement for sustained EBFC operation. To date, none of these methods have been successfully applied to hydrogel-based EBFC electrodes, underscoring a major barrier to developing high-performance hydrogel bioelectrodes [47–50].

In this study, we introduce a micro-corrugated hydrogel electrode for high-performance EBFC, which delivers both high power output and long-term operational stability through capillary force- and interfacial interaction-driven in situ assembly of metal NPs onto the wet hydrogel surface and enzyme layer (Figure 1). These combined strategies enable the formation of a hydrogel host electrode with bulk metal-like electrical conductivity (~8.4×10^{4} S cm^{-1}), micro-corrugated structure, robust mechanical integrity, and strong enzyme immobilization through a simple, scalable dipping deposition method. Critically, the enzyme immobilization used in our system is not based on weak physical adsorption, but instead driven by strong interfacial interactions—specifically, covalent bonding—between the hydrogel surface and amino acid functional groups of the enzymes, thereby ensuring stability and activity of the immobilized enzymes.

To fabricate the highly conductive hydrogel, we first synthesized a copolymerized poly(acrylic acid)-poly(acrylamide) (PAA-co-PAAm) hydrogel incorporating poly(ethylene imine) (PEI), which was then immersed in a toluene solution containing tetra(octylammonium) (TOA)-stabilized Au nanoparticles (TOA-Au NPs). This process led to the formation of vertically and laterally dense Au NP arrays on the hydrogel surface, driven by continuous capillary transport and ligand exchange reactions

16136829, 2026, 14, Downloaded from https://onlinelibrary.wiley.com/doi/10.1002/smll.202512318 by Kangwon National University, Wiley Online Library on [08/03/2026]. See the Terms and Conditions (https://onlinelibrary.wiley.com/terms-and-conditions) on Wiley Online Library for rules of use; OA articles are governed by the applicable Creative Commons License

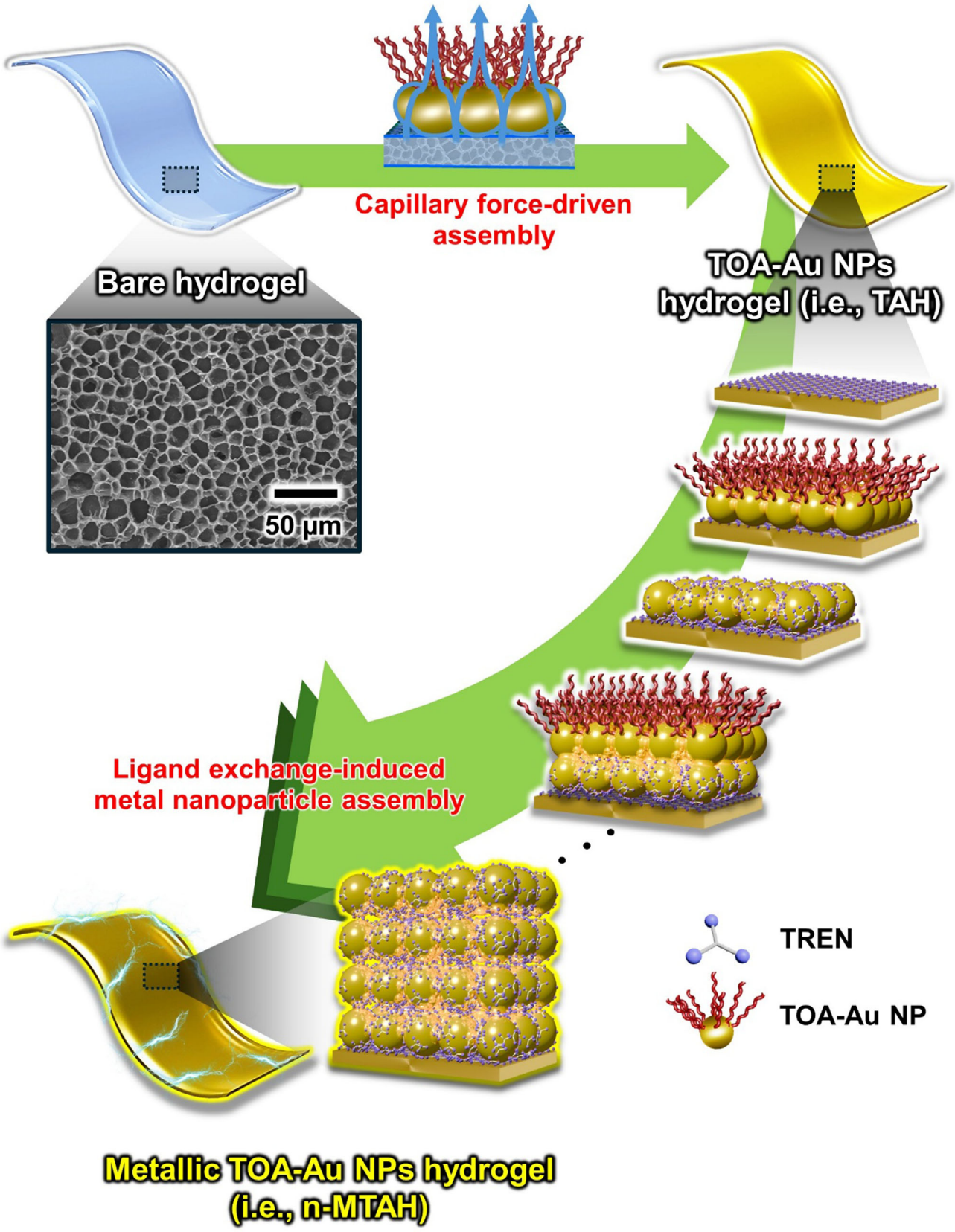

FIGURE 1 | Schematic illustration of the metallic TOA-Au NPs hydrogel (n-MTAH) using capillary force and ligand exchange-induced metal nanoparticle assembly.

16136829, 2026, 14, Downloaded from https://onlinelibrary.wiley.com/doi/10.1002/smll.202512318 by Kangwon National University, Wiley Online Library on [08/03/2026]. See the Terms and Conditions (https://onlinelibrary.wiley.com/terms-and-conditions) on Wiley Online Library for rules of use; OA articles are governed by the applicable Creative Commons License

(LER) between the NH_2-functionalized PEI within the aqueous-phase hydrogel and the weakly bound TOA ligands on the Au NPs dispersed in the nonpolar solvent. The resulting electrode achieved a high electrical conductivity of approximately 8.4×10^4 S cm^{-1}, surpassing all previously reported hydrogel electrodes, including ion-embedded hydrogels [51–54], conductive polymer-incorporated hydrogels [36–40], conductive filler-incorporated hydrogels [30–35], and conductive material-coated hydrogels [42–45, 55] (Table S1).

For the EBFC anode, GOx was layer-by-layer (LbL) assembled with TOA-Au NPs onto the conductive hydrogel via the same LER mechanism, where the NH_2 groups in the amino acid residues of enzyme interact with the TOA ligands. For the cathode, Pt—chosen for its excellent oxygen reduction reaction (ORR) activity—was deposited onto the conductive hydrogel to complete the device architecture. The resulting hybrid-type EBFCs, composed of a covalently enzyme-linked hydrogel anode and a Pt-modified hydrogel cathode, exhibited a maximum areal power density of ~3.7 mW cm^{-2} with an OCV of 0.95 V at a glucose concentration of 300 mmol L^{-1}. Even under physiological glucose conditions (10 mmol L^{-1}), the EBFCs maintained an impressive areal power density of ~2.4 mW cm^{-2}, with an OCV of approximately 0.92 V. Furthermore, the devices retained approximately 80% of their initial power output (corresponding to 1.9 mW cm^{-2}) after 30 days of continuous operation, confirming their excellent operational durability. We believe that our approach establishes a promising design platform for hydrogel-based EBFCs, offering not only efficient electron transfer and strong enzyme retention, but also long-term reliability, which are essential for future bioelectronic and biomedical applications.

2 | Results and Discussion

2.1 | Design and Preparation of Hydrogel Electrodes

To prepare conductive hydrogel host electrode (Figure 2a), we first synthesized a PAA-co-PAAm hydrogel template (Figure S1). This template was subsequently immersed in NH_2-functionalized PEI (M_w ~800) solution at pH 11, with a concentration of 20 mg mL^{-1}, to incorporate PEI into the hydrogels. At this alkaline pH, a significant portion of the carboxylic acid (COOH) groups in PAA component (pK_a of PAA ~4.5, i.e., the pH at which 50% of the groups are ionized) of the hydrogels were deprotonated to form carboxylate ions (COO^-), while the PEI component (pK_a ~10.5) remained partially protonated. The resulting electrostatic repulsion between the same negatively charged COO^- groups caused the hydrogel to swell to more than six times its original volume (Figure S2).

On the other hand, hydrogels prepared using high-molecular-weight PEI (Mw ~ 25,000) (i.e., PEI ~ 25,000-hydrogel) exhibited a markedly reduced swelling ratio (~113%) compared to those prepared with low-molecular-weight PEI (Mw ~ 800) (i.e., PEI ~ 800-hydrogel). This diminished swelling behavior indicates the formation of a denser polymer network, likely arising from the limited diffusivity and restricted mobility of the longer PEI chains within the hydrogel matrix (Figure S3). Consistent with this interpretation, the PEI ~ 25,000-hydrogel displayed a significantly higher Young's modulus (~360 kPa) than the PEI ~ 800-hydrogel (~65 kPa), confirming the emergence of a much stiffer and less compliant network structure (Figure S4).

Based on these results, the swollen PEI-hydrogel was subsequently immersed in a toluene solution containing TOA-Au NPs with diameters of approximately 8 nm (Figure S5). This treatment resulted in the formation of dense Au NP layers on the surface of the PEI-hydrogel. Concurrently, the hydrogel underwent substantial deswelling, with the final volume of the Au NP-assembled PEI-hydrogel reduced to approximately 31% of its initial swollen state (Figure S2). Additionally, as the deposition time of the Au NPs increased, the initially adsorbed Au NPs were gradually transformed into porous Au nanoplate films composed of numerous Au NPs. This transformation led to a notable increase in film thickness—from ~67 nm (after 12 h) to ~149 nm (after 72 h) (Figure 2b). It was reported that for Ag or Au NPs with low cohesive energy, the strong metallic bonding between adjacent metal NPs can occur when the inter-particle separation is less than 5–7 Å [56–59]. Furthermore, TOA-Au NPs-based hydrogel electrode (shortly, TAH electrode) featured a uniquely micro-corrugated surface morphology as confirmed by field-emission scanning electron microscopy (FE-SEM) image (Figure 2c). In contrast, when high-molecular-weight PEI (Mw ~ 25,000) was used (i.e., PEI ~ 25,000-hydrogel), the Au nanoplates became significantly thicker—from ~215 nm at 12 h to ~820 nm at 72 h—reflecting more pronounced nanoparticle aggregation and film coarsening. This excessive thickening impaired electrical transport (Figure S6), leading to markedly lower electrical conductivity (~2.2×10^4 S cm^{-1}) compared with the PEI ~ 800-based hydrogel. Such reduced conductivity is attributed to hindered ligand exchange and the suppressed formation of continuous, well-connected Au pathways within the dense polymer network (Figure S7).

This increase in Au nanoplate thickness and unique morphological evolution are primarily attributed to the NH_2 groups in the incorporated PEI of TAH, which exhibit stronger binding affinity toward Au NP surfaces than the ammonium groups of the native TOA ligands. Specifically, the loosely bound TOA ligands on Au NP surfaces were replaced by NH_2 groups of PEI at the water/toluene interface through a continuous ligand exchange reaction. Moreover, the continuous capillary-driven transport of PEI from the hydrogel interior to the outer TOA-Au NP layers sustained this ligand exchange process, thereby facilitating the growth of thick and interconnected Au nanoplate films. In contrast, in the case of spin-coated TOA-Au NP-coated film without ligand exchange, the interparticle interface between neighboring TOA-Au NPs is composed of two bulky TOA ligand layers (M_w of TOA ~546), which prevent close contact. As a result, this film did not undergo fusion at room temperature and was expected to exhibit electrically insulating behavior, with a sheet resistance exceeding ~10^7 Ω sq^{-1}.

These observations were further supported by experiments conducted using a two-phase liquid system composed of an aqueous PEI solution (in water) and a toluene-based TOA-Au NP dispersion (in toluene). As shown in Figure 2d, the dispersed TOA-Au NPs gradually assembled into Au nanoplate layers at the water/toluene interface. This transformation was driven by a LER at the NP surfaces, in which the hydrophobic TOA ligands were

16136829, 2026, 14, Downloaded from https://onlinelibrary.wiley.com/doi/10.1002/smll.202512318 by Kangwon National University, Wiley Online Library on [08/03/2026]. See the Terms and Conditions (https://onlinelibrary.wiley.com/terms-and-conditions) on Wiley Online Library for rules of use; OA articles are governed by the applicable Creative Commons License

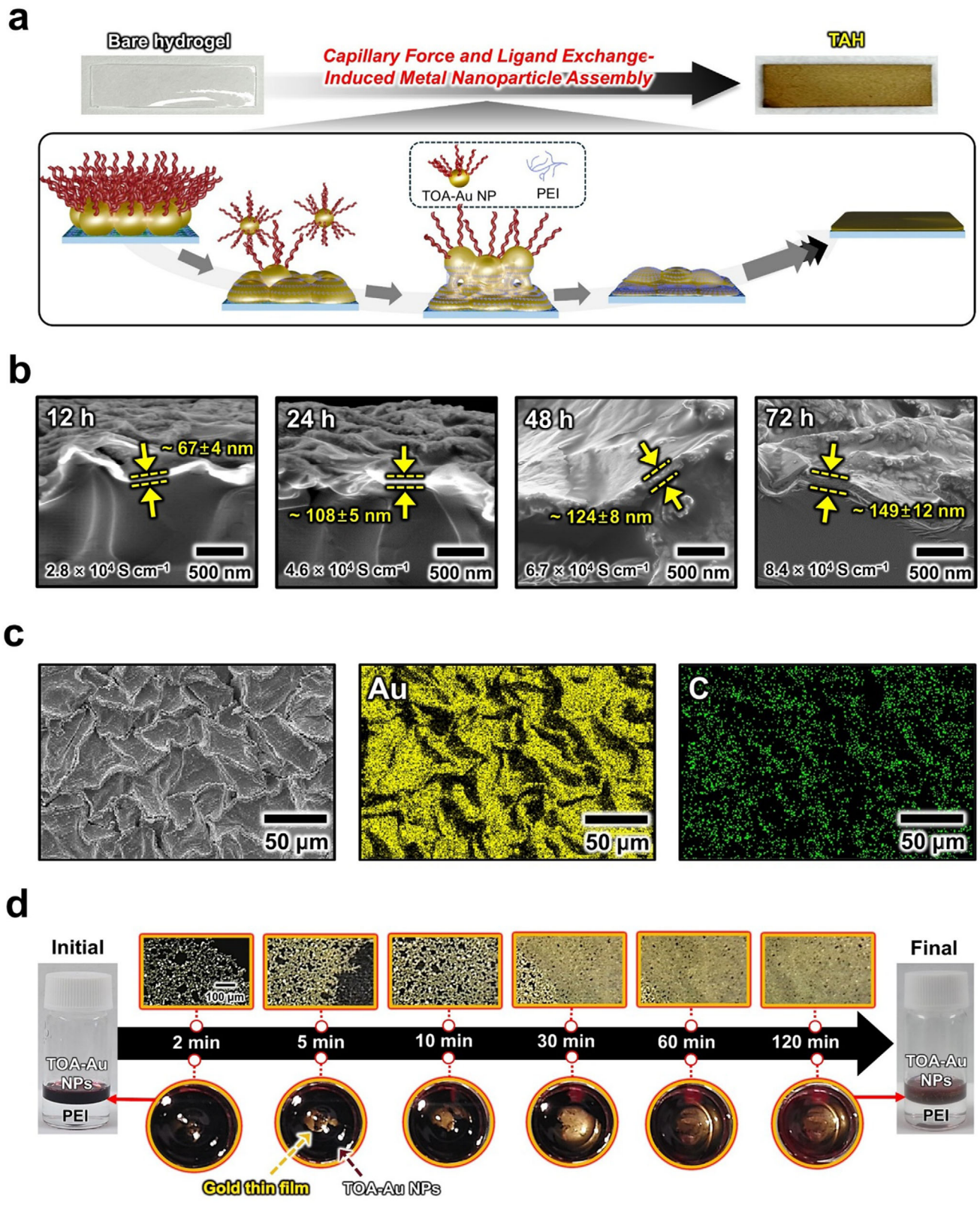

FIGURE 2 | Characterization of TOA-Au NPs hydrogel (i.e., TAH). (a) Fabrication of TAH. (b) Gradual formation of porous Au NP films, with thickness increasing from 67 nm (12 h) to 149 nm (72 h). (c) FE-SEM image of TAH electrode showing micro-corrugated surface morphology. (d) Capillary-assisted in situ assembly and PEI-driven formation of sintered gold thin films on hydrogel.

16136829, 2026, 14, Downloaded from https://onlinelibrary.wiley.com/doi/10.1002/smll.202512318 by Kangwon National University, Wiley Online Library on [08/03/2026]. See the Terms and Conditions (https://onlinelibrary.wiley.com/terms-and-conditions) on Wiley Online Library for rules of use; OA articles are governed by the applicable Creative Commons License

replaced by hydrophilic PEI molecules. As a result, the surface character of the Au NPs shifted from hydrophobic to hydrophilic, significantly enhancing capillary-driven PEI transport toward the upper, initially hydrophobic TOA-Au NP layers. Moreover, the real-time interfacial observations provided clearer insight into the dynamic kinetics of this assembly process and offered complementary evidence reinforcing the validity of our proposed capillary-driven mechanism (Movie S1). This capillary action—closely resembling the mechanism observed in the hydrogel system—enabled continuous sintering of the Au NPs, leading to the formation of porous Au nanoplate structures at the interface. As a result, both the vertical and lateral dimensions of the resulting Au NP film increased progressively as the ligand exchange and sintering processes continued.

To further validate the interfacial chemistry governing this assembly process, we performed time-resolved Attenuated total reflection Fourier transform infrared (ATR-FTIR) spectroscopy during TOA–Au NP deposition. The TOA-derived C–H stretching bands (2,850–2,920 cm^{-1}) gradually decreased in intensity, confirming progressive TOA-to-PEI ligand substitution. By normalizing the 10-min spectrum to 100%, the degree of exchange (DOE) was found to increase from ~23% at 30 min to ~57% at 120 min, demonstrating a time-dependent substitution process approaching saturation (Figure S8). Complementary X-ray photoelectron spectroscopy analysis further corroborated this mechanism, revealing the stepwise emergence of Au–N coordination, attenuation of the Br 3d signal, and preservation of the metallic Au^0 state. Together, these spectral trends verify the gradual replacement of TOA ligands by PEI during nanoplate growth (Figure S9).

In contrast to previously reported NP assembly methods—which typically yield either low-packing density monolayers or electrostatic interaction-based multilayers through a few hundreds of multiple deposition steps [60–62]—our capillary force-induced metal NP assembly strategy offers distinct advantages, in terms of electrical and mechanical properties, by enabling the direct and robust formation of conductive components on wet hydrogel substrates. Using this approach, the resulting conductive hydrogels displayed remarkably high electrical conductivity (~8.4×10^4 S cm^{-1}) and low sheet resistance (0.8 Ω sq^{-1}) after 72 h of immersion (Figure 3a). The micro-corrugated architecture generated during capillary-induced assembly also plays a key role in enhancing electrochemical performance. As the Au nanoplate layer becomes progressively thicker with increasing immersion time, the areal current density rises substantially—from 0.8 mA cm^{-2} at 12 h to 3.0 mA cm^{-2} at 72 h (Figure S10a,b). This structural evolution is accompanied by improvements in electrical transport, reflected in increased conductivity and a decrease in equivalent series resistance (ESR) from 1.5×10^2 Ω at 12 h to 1.1×10^2 Ω at 72 h (Figure S10c).

For comparison, we also fabricated the hydrogel host electrode through electrostatic interaction between the NH_3^+ groups of PEI and the COO^- groups of citrate ion-stabilized Au NPs (i.e., anionic Au NPs) dispersed in pH 4 water. However, this method failed to generate densely packed Au NP arrays on the hydrogel template due to the electrostatic repulsion between the same charged Au NPs, resulting in significantly inferior electrical performance. Specifically, the citrate Au NPs-based hydrogel electrode exhibited extremely low conductivity (~2.0×10^{-3} S cm^{-1}) and high sheet resistance (~1.2×10^6 Ω sq^{-1}) (Figure S11). Additionally, this hydrogel electrode exhibited relatively flat and smooth surface morphology due to extremely low packing density (< 30%) [62, 63] of electrostatic interaction-induced Au NP arrays, which was in stark contrast to the TAH with the swelling-deswelling-induced micro-corrugated surface morphology.

With their excellent electrical characteristics, the TAH electrodes exhibited remarkable mechanical flexibility. They retained their conductive properties during both bending (with a bending radius (R) of ~1 mm) and stretching conditions. Notably, the TAH electrode maintained its electrical performance over 10000 cycles of 100% uniaxial stretching at a strain rate of 1 s^{-1}, demonstrating exceptional durability under repetitive mechanical deformation (Figure 3b,c). Furthermore, the TAH electrodes endured a variety of deformations—including bending, crumpling, twisting, and stretching—without compromising structural integrity (Figure S12). These results clearly demonstrate that the TAH assembled from densely packed TOA-Au NPs achieves outstanding electrical conductivity, outperforming not only the citrate Au NPs-based hydrogel but also most previously reported conductive hydrogels, as summarized in Figure 3d and Table S1. Notably, TAH maintains its high conductivity even under applied strain, demonstrating excellent mechanical–electrical stability for flexible bioelectronic applications. In addition to the 10,000-cycle durability assessment, the electrochemical stability of the TAH was further evaluated under mechanically deformed conditions. During cyclic release–stretch operation (0–50% strain), the TAH exhibited highly consistent cyclic voltammetry (CV) responses, showing less than a 22% decrease in anodic current density over the first 20 cycles. This result confirms that the electrode maintains stable charge-transfer characteristics even under dynamic mechanical strain (Figure S13).

The micro-corrugated structure of the TAH is expected to offer superior electrochemical performance as a host electrode compared to conventional electrodes with flat and smooth structures. First, as confirmed by FE-SEM and optical microscopy, the TAH exhibited a distinct corrugated structure, in stark contrast to the flat surface of the citrate Au NPs-based hydrogel prepared via electrostatic interactions (Figure 4a,b; Figure S14). This unique structure arises from the capillary-assisted assembly of TOA-Au NP on the PEI-hydrogel, followed by swelling–deswelling dynamics. Notably, the corrugated structure of the TAH can enhance the electrochemical performance of the electrode by increasing the effective surface area at the electrode-electrolyte interface.

For confirming this possibility, we compared the electrochemical performance of the TAH with that of a citrate Au NPs-based hydrogel. Although Au nanoparticles inherently produce a small background oxidation current in phosphate-buffered saline (PBS) due to their intrinsic surface redox activity, this contribution is negligible relative to the catalytic response of the TAH. As shown in Figure 4c and Figure S15, the TAH exhibited a markedly higher areal current density of 3.0 mA cm^{-2} at +0.6 V, whereas the citrate–Au NP hydrogel generated only 5.2×10^{-4} mA cm^{-2}. This stark contrast confirms that the electrochemical response of the TAH arises predominantly from its engineered micro-corrugated

16136829, 2026, 14, Downloaded from https://onlinelibrary.wiley.com/doi/10.1002/smll.202512318 by Kangwon National University, Wiley Online Library on [08/03/2026]. See the Terms and Conditions (https://onlinelibrary.wiley.com/terms-and-conditions) on Wiley Online Library for rules of use; OA articles are governed by the applicable Creative Commons License

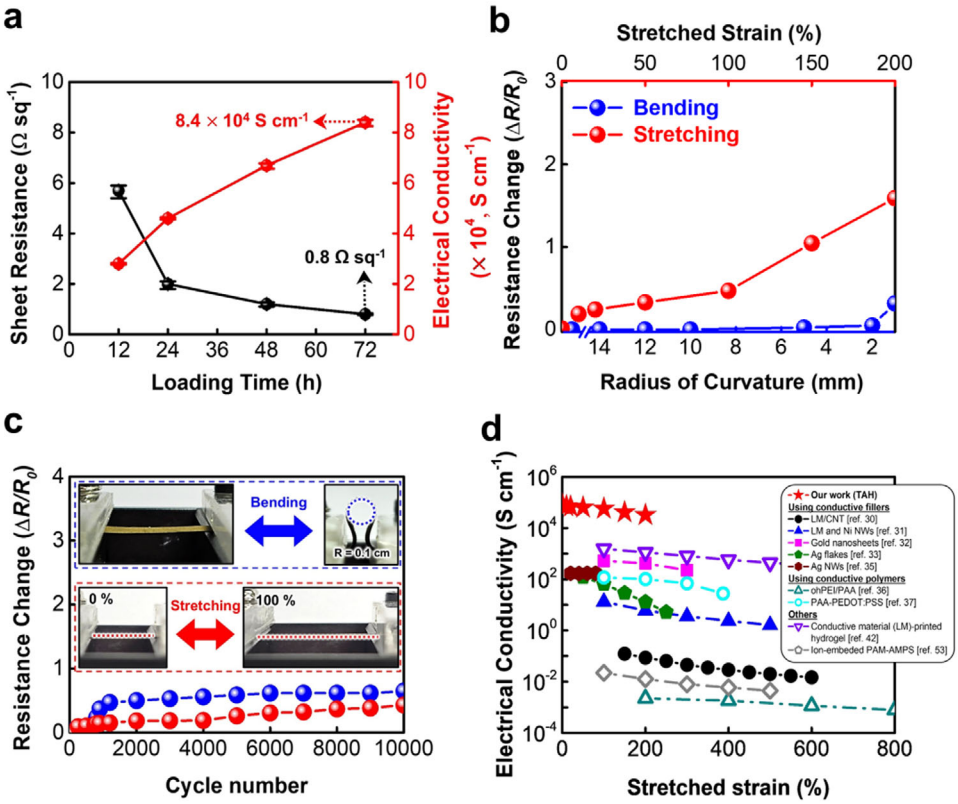

FIGURE 3 | Characterization of TAH. (a) Loading time-dependent evolution of sheet resistance and electrical conductivity. (b) Comparison of electrical conductivity and stretchability between TAH (our study) and previously reported hydrogel-based electrodes. (c) Resistance changes ($\Delta R/R_0$) in TAH as a function of bending (blue) and stretching (red) radius (R). (d) Resistance changes ($\Delta R/R_0$) and photographs (insets) of TAH under bending (blue) and stretching (red), during 10000 cycles at a tensile strain of 100%.

conductive architecture rather than from the intrinsic faradaic activity of Au NPs.

Furthermore, electrochemical impedance spectroscopy (EIS) revealed additional advantages of the TAH. Specifically, it exhibited a much lowerESR of 1.1×10^2 Ω compared to ~4.2×10^4 Ω for the citrate Au NPs-based hydrogel (Figure 4d; Figure S16). The TAH also displayed a steeper Warburg slope in the low-frequency region, indicating enhanced ion diffusion and charge transport behavior. In long-term stability tests conducted over 30 days in PBS, the TAH maintained 72% of its initial current density, whereas the citrate Au NPs-based hydrogel retained only ~18% (Figure 4e; Figure S17), further demonstrating the superior operational durability of the TAH.

To further assess the structural merits of our approach, we also prepared a control electrode by sputtering a thin Au layer directly onto the hydrogel (i.e., Au-sputtered hydrogel). While this control electrode exhibited high electrical conductivity (~2.2×10^2 S cm^{-1}) and low sheet resistance (0.2 Ω sq^{-1}) (Figure S11), its electrochemical performance was poor, with a low areal current density of only 7.5×10^{-2} mA cm^{-2} and a relatively high ESR of ~4.3×10^2 Ω (Figures S15c and S16c). Moreover, severe surface delamination and degradation were observed during electrochemical operation, significantly undermining both performance and stability (Figures S17 and S18). These structural failures render the Au-sputtered hydrogel unsuitable as a reliable host electrode for electrochemical applications.

The structural durability of the TAHs was evaluated through a rigorous 100-day cyclic test involving repeated air-drying and immersion in PBS (Figure S19a). The TAHs demonstrated excellent resilience, retaining 81% of its initial conductivity (6.8×10^4 S cm^{-1}) after 30 days and 63% (5.3×10^4 S cm^{-1}) after 100 days. Upon re-immersion in PBS, partial reswelling occurred, which slightly reduced the electrical conductivity but fully preserved the overall corrugated architecture (Figure S19b,c). This reversible structural response highlights the hydrogel's robustness and adaptability under prolonged environmental stress. Additionally, the outstanding electrical performance of the TAH is primarily attributed to its interconnected and micro-corrugated Au nanoplate. This unique integration of high electrical conductivity, mechanical integrity, and long-term stability can position the TAH as a highly promising electrode platform for high-performance bioelectrochemical systems and other flexible energy devices.

Based on these results, we sought to further enhance the electrical conductivity of conductive TAH. To achieve this, the TOA-Au NPs were additionally assembled onto the TAH via a LbL assembly process using NH_2-functionalized small molecular linkers, such as tris-(2-aminoethyl)amine (TREN) (M_w ~146). In this case, bulky TOA groups loosely bound to the Au NP surface were replaced by NH_2 groups of TREN through LER—similar to the previously described system involving PEI-hydrogel and TOA-Au NPs—which was confirmed by FTIR spectroscopy (Figure S20). This additional LbL assembly of TOA-Au NPs with TREN significantly improved the electrical conductivity of the TAH by

16136829, 2026, 14, Downloaded from https://onlinelibrary.wiley.com/doi/10.1002/smll.202512318 by Kangwon National University, Wiley Online Library on [08/03/2026]. See the Terms and Conditions (https://onlinelibrary.wiley.com/terms-and-conditions) on Wiley Online Library for rules of use; OA articles are governed by the applicable Creative Commons License

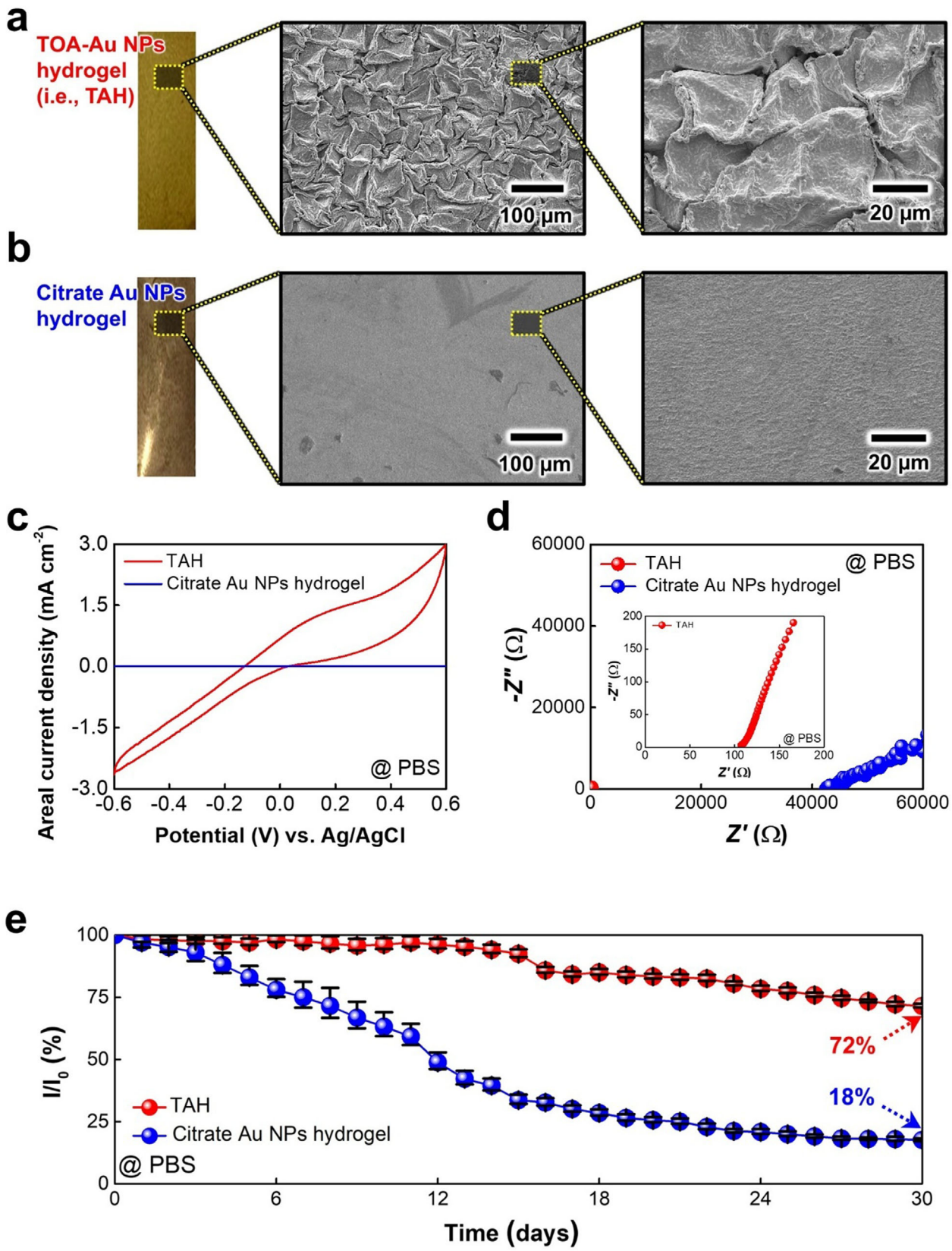

FIGURE 4 | Comparison of Au-based hydrogel, such as TAH and citrate Au NPs hydrogel. (a) Photograph (left side) and planar FE-SEM images of TAH. (b) Photograph (left side) and planer FE-SEM images of citrate Au NPs hydrogel. (c) CV curves of Au-based hydrogels in PBS solution. (d) Nyquist plots of Au-based hydrogels in PBS solution. The inset shows the magnified Nyquist plot of TAH, highlighting its significantly lower impedance compared to the citrate Au NPs hydrogel. (e) Long-term stability of each Au-based hydrogel in PBS solution over 30 days. The TAH retained 72% of its initial current density ($I_0 = 3.0$ mA cm^{-2}, $I = 2.1$ mA cm^{-2}), showing superior long-term stability. In contrast, the citrate Au NPs hydrogel maintained only 18% ($I_0 = 5.2 \times 10^{-4}$ mA cm^{-2}, $I = 9.4 \times 10^{-5}$ mA cm^{-2}).

16136829, 2026, 14, Downloaded from https://onlinelibrary.wiley.com/doi/10.1002/smll.202512318 by Kangwon National University, Wiley Online Library on [08/03/2026]. See the Terms and Conditions (https://onlinelibrary.wiley.com/terms-and-conditions) on Wiley Online Library for rules of use; OA articles are governed by the applicable Creative Commons License

facilitating the displacement of terminal TOA ligands, thereby promoting closer interparticle contact and reducing interfacial resistance. Additionally, increasing the bilayer number (n) of $(TOA\text{-}Au\ NP/TREN)_n$ multilayers on the TAH from 1 to 5 led to a significant enhancement in the electrical conductivity of the resulting $(TOA\text{-}Au\ NP/TREN)_n$/TAH electrodes, with values rising from ~1.1×10^5 to ~1.5×10^5 S cm^{-1} (Figure S21), approaching those of bulk metals. This metallic TOA-Au NPs hydrogel electrode is hereafter referred to as n-MTAH, where n denotes the number of TOA-Au NP/TREN bilayers. Although further increasing the bilayer number may improve electrical conductivity even more, the maximum bilayer number was limited to 5 in consideration of fabrication efficiency and process scalability. The electrode with five bilayers ($n = 5$) is hereafter referred to as 5-MTAH.

Building on these findings, we further evaluated the mechanical properties of the PEI-hydrogel, TAH, and highly conductive 5-MTAH electrodes by analyzing their stress–strain profiles (Figure S22). First, the PEI-hydrogel exhibited a Young's modulus of 65 kPa and an elongation-at-break of approximately 289%, indicating excellent softness and stretchability. Additionally, TAH demonstrated a young's modulus of 181 kPa and an elongation-at-break of approximately 222%. To elucidate the influence of PEI molecular weight, we directly compared TAH electrodes fabricated using PEI ~ 800 and PEI ~ 25,000. Consistent with the denser polymer network formed by high–molecular-weight PEI, the TAH based on PEI ~ 25,000 exhibited substantially increased stiffness and reduced stretchability (Figure S23). On the other hand, the 5-MTAH electrode, in which the Au nanoplates were further fused and thickened, displayed a slightly higher modulus (182 kPa) and a reduced elongation-at-break (~222%). This mechanical behavior is attributed to the presence of rigid, interconnected Au nanoplate domains, which significantly enhance electrical conductivity but moderately compromise flexibility. Nevertheless, the n-MTAH electrodes maintain a favorable balance between mechanical compliance and electrical performance. These results collectively underscore the multifunctional characteristics of the hydrogel-based electrode—offering high electrical conductivity, mechanical durability, and a large electroactive surface area—which position it as a promising platform for next-generation wearable energy systems, particularly for highly flexible and stretchable EBFCs.

2.2 | Preparation and Performance of Hydrogel Anode

Based on these results, we fabricated hydrogel-based anodes (for EBFC) by performing repetitive LbL assembly of GOx (in water) and TOA-Au NPs (in toluene) onto 5-MTAH host electrode. In this configuration, the TOA-Au NPs serve as conductive linkers bridging vertically adjacent GOx layers, thereby facilitating efficient electron transport throughout the multilayered structure (Figures 1 and 5a).

First, we evaluated the electrochemical performance of n-MTAH host electrodes with varying bilayer numbers ($n = 1$ to 5) using CV at a scan rate of 5 mV s^{-1} in PBS (20 mmol L^{-1}, pH 7.4) under ambient conditions. As the bilayer number (n) of $(TOA\text{-}Au\ NP/TREN)_n$ multilayers increased, the anodic current density at +0.6 V progressively rose from 3.2 mA cm^{-2} ($n = 1$) to 3.8 mA cm^{-2} ($n = 5$), which can be attributed to the increased electroactive surface area provided by the additional Au NP layers (Figure S24a,b). EIS analysis supported these observations, showing a consistent decrease in ESR from approximately 98 Ω ($n = 1$) to 60 Ω ($n = 5$) (Figure S24c). These results collectively indicate enhanced electron transfer kinetics and reduced overall impedance with increasing bilayer number. Based on these findings, 5-MTAH was selected as the optimized host electrode for the preparation of anode via GOx immobilization.

Subsequently, GOx was immobilized onto the 5-MTAH electrode via additional LbL assembly with TOA-Au NPs, forming $(GOx/TOA\text{-}Au\ NP)_m$ multilayers. The resulting hydrogel-based anode is hereafter referred to as m-GOx-5-MTAH. This assembly was conducted in PBS at room temperature. Notably, the NH_2 moieties of the amino acid residues in GOx exhibit strong affinity toward the Au NP surface, thereby facilitating ligand exchange between GOx and the weakly bound TOA ligands on the nanoparticles. This substitution process results in the formation of interfacial amide/N–Au covalent (or coordination) bonds, as evidenced by the reciprocal spectral evolution observed in the UV–vis and FTIR analyses (Figures S25 and S26). Furthermore, QCM measurements reveal a continuous increase in adsorbed mass with increasing bilayer number, consistent with the progressive formation of N–Au bonds and the corresponding accumulation of GOx on the electrode surface (Figure S27).

Importantly, our method enables direct interfacial contact between conductive Au NPs and GOx without relying on insulating organic linkers (e.g., bulky ligands bound to the Au NP surface) or polymeric binders. Unlike electrostatically stabilized metal NPs in aqueous media, which often suffer from strong electrostatic repulsion, the hydrophobic TOA-Au NPs dispersed in nonpolar solvents such as toluene exhibit negligible interparticle repulsion. This allows for their dense and uniform assembly onto the GOx layer. It is also noteworthy that the TOA-Au NP layers used to construct the amphiphilic LbL multilayers composed of hydrophilic GOx and hydrophobic TOA-Au NPs were the same as those applied to the 5-MTAH, with the added feature that GOx was nanoblended with Au NPs in both the vertical and lateral dimensions (Figure 5a). This unique structural integration suggests that electron transfer can be significantly enhanced not only between adjacent GOx molecules but also between GOx and the underlying 5-MTAH, compared to conventional slurry-cast GOx films.

To further validate this possibility, we investigated the electrochemical behavior of the m-GOx-5-MTAH (Figure 5b,c; Figure S28). As the bilayer number (m) of m-GOx-5-MTAH increased from 1 to 7, the anodic current density showed a marked increase up to m = 5, followed by a gradual decline (Figure 5b; Figure S29). Concurrently, the ESR of m-GOx-5-MTAH exhibited a modest rise from approximately 59 Ω (m = 0) to approximately 127 Ω (m = 7) at 300 mmol L^{-1}, suggesting that excessive multilayer formation introduces resistive interfaces that hinder efficient electron transfer (Figure 5c). The electrocatalytic response of 5-GOx-5-MTAH was further evaluated as a function of glucose concentration (0–300 mmol L^{-1}) in PBS (pH 7.4). As the glucose concentration increased, the anodic current density progressively rose (Figure 5d), indicating the enhanced catalytic oxidation of

16136829, 2026, 14, Downloaded from https://onlinelibrary.wiley.com/doi/10.1002/smll.202512318 by Kangwon National University, Wiley Online Library on [08/03/2026]. See the Terms and Conditions (https://onlinelibrary.wiley.com/terms-and-conditions) on Wiley Online Library for rules of use; OA articles are governed by the applicable Creative Commons License

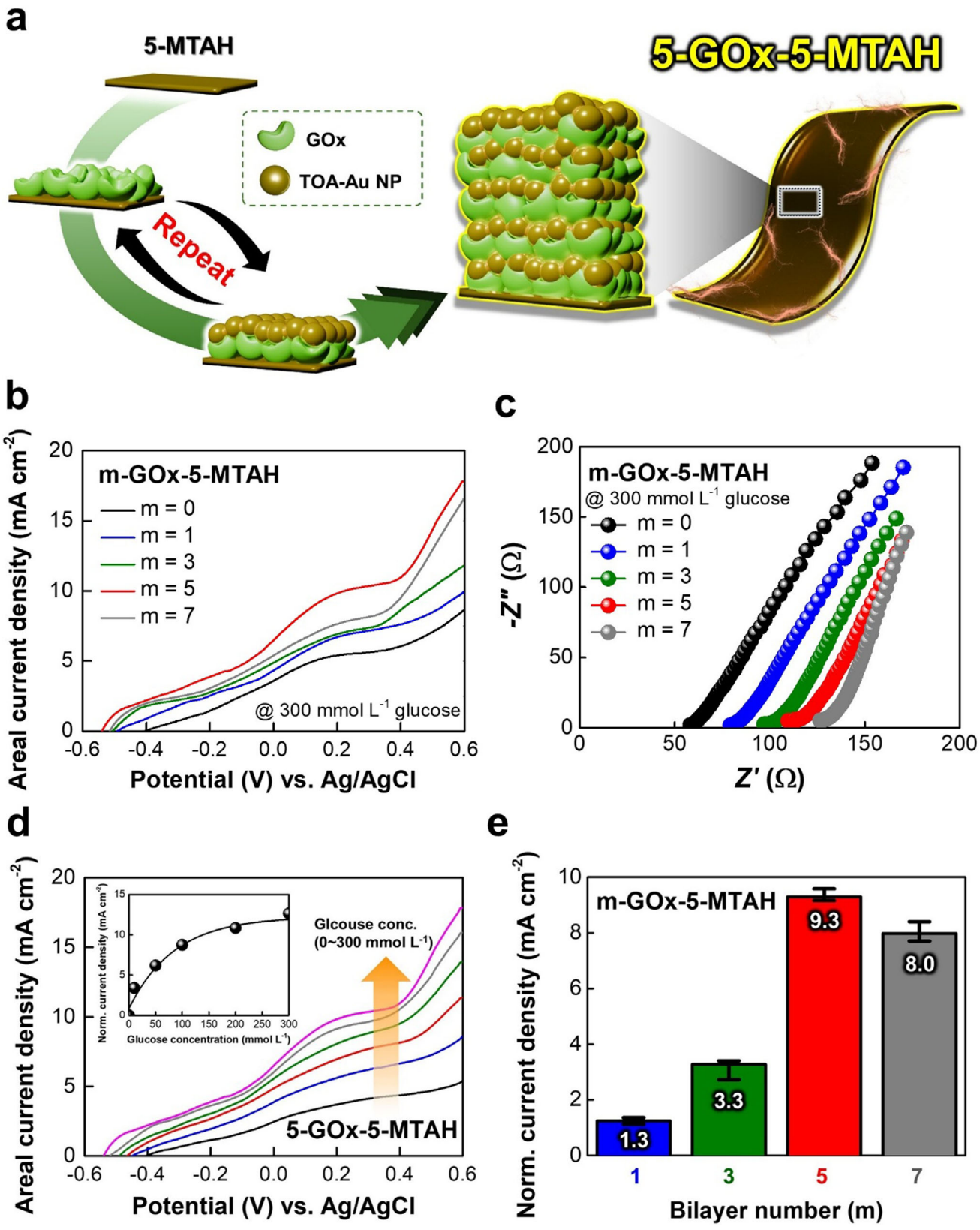

FIGURE 5 | Electrochemical performance of m-GOx-5-MTAH. (a) Schematic illustration of the 5-GOx-5-MTAH. (b) Anodic current densities of m-GOx-5-MTAH as a function of the bilayer number (m) at a scan rate of 5 mV s^{-1} in PBS solution containing 300 mmol L^{-1} glucose at 36.5°C. (c) Nyquist plots of m-GOx-5-MTAH depending on the bilayer number. (d) Anodic current densities of the 5-GOx-5-MTAH with increasing glucose concentrations (0–300 mmol L^{-1}), as further confirmed by the normalized anodic current densities at +0.6 V shown in the inset. (e) Normalized anodic current densities of m-GOx-5-MTAH as function of the bilayer number.

16136829, 2026, 14, Downloaded from https://onlinelibrary.wiley.com/doi/10.1002/smll.202512318 by Kangwon National University, Wiley Online Library on [08/03/2026]. See the Terms and Conditions (https://onlinelibrary.wiley.com/terms-and-conditions) on Wiley Online Library for rules of use; OA articles are governed by the applicable Creative Commons License

glucose by GOx. This correlation was further supported by the normalized current density values, which were obtained after subtracting background signals measured in glucose-free PBS at +0.6 V. In parallel, the ESR values were evaluated over the same glucose concentration range, revealing a slight increase as the glucose concentration increased from 0 to 300 mmol L^{-1}. This increase is attributed to electron transfer associated with the glucose oxidation reaction (Figure S30). More specifically, higher glucose concentrations accelerate the catalytic turnover of GOx, thereby increasing the exchange current density and reducing the diffusion impedance, as evidenced by the more flattened Warburg tail. Concurrently, the faster reaction rate induces localized ionic redistribution at the hydrogel–electrolyte interface, which slightly decreases the local ionic conductivity and leads to a modest increase in the high-frequency series resistance.

Additionally, to elucidate the influence of bilayer number on catalytic performance, we systematically investigated the normalized anodic current density across m = 1 to 7 (Figure 5e). A consistent increase was observed, from 1.3 mA cm^{-2} at m = 1 to a peak of 9.3 mA cm^{-2} at m = 5, indicating that progressive LbL assembly significantly enhances GOx activity. Notably, the 5-GOx-5-MTAH electrode exhibited a maximum areal current density of 17.9 mA cm^{-2}, affirming that the observed enhancement is primarily attributed to glucose oxidation catalyzed by GOx. However, further increasing the bilayer number to m = 7 resulted in a reduced areal current density of 16.5 mA cm^{-2}, due to mass transport limitations, increased steric hindrance, or elevated interfacial resistance within the overly thick multilayer structure. The active-enzyme surface coverage of the optimized m-GOx-5-MTAH electrode (m = 5) was determined to be 2.1×10^{-8} mol cm^{-2}, which corresponds well with values reported for densely packed enzyme multilayers in high-performance EBFC systems [19, 64]. These findings suggest that a bilayer number of m = 5 offers the optimal configuration for maximizing electron transfer efficiency and catalytic performance, highlighting the critical role of LbL engineering in fine-tuning enzymatic electrode architectures.

To further explore the electron transfer kinetics of the optimized 5-GOx-5-MTAH, the Laviron model was applied to estimate the apparent heterogeneous electron transfer rate constant (k_s) [65]. The CV was performed at various scan rates (ν), and the resulting anodic and cathodic peak current densities increased linearly with scan rate, indicating a surface-controlled quasi-reversible redox process (Figure S31a,b). With increasing the scan rate, the peak-to-peak potential separation ($\Delta E_p = E_{pa}—E_{pc}$) also increased. A linear relationship between ($E—E^0$) and log(ν) allowed extraction of k_s value (Figure S31c), yielding 3.7 ± 0.2 s^{-1} for 5-GOx-5-MTAH—indicating efficient catalytic kinetics at the electrode–enzyme interface. This high rate constant is supported by a relatively small ΔE_p of 83 mV at a scan rate of 100 mV s^{-1}, and it surpasses values reported for other electrode systems such as carbon nanomaterials (2.1 s^{-1}) [66], conducting polymers (2.2 s^{-1}) [67], and metal–organic composites (1.1 s^{-1}) [68]. In surface-controlled electrochemical systems, a ΔE_p below 200 mV generally reflects a fast heterogeneous electron transfer process; thus, the small ΔE_p observed here confirms effective enzyme immobilization and rapid electron exchange at the bioelectrode interface [65]. Moreover, to evaluate the catalytic activity and substrate affinity of the immobilized enzyme under low-glucose conditions, we analyzed the current response of the 5-GOx-5-MTAH anode using the Michaelis–Menten model and constructed a Lineweaver–Burk plot [69]. The 5-GOx-5-MTAH electrode exhibited a linear current response to glucose in the range of 0–10 mmol L^{-1} (Figure S32). From the slope and intercept of the Lineweaver–Burk equation, the Michaelis–Menten constant K_M^{app} was estimated to be approximately 3.4 mmol L^{-1}, indicating that the immobilized GOx retained a strong affinity toward glucose. To assess the effect of multilayer assembly on the electron transfer rate, the k_s values were additionally determined for the 1-GOx-5-MTAH (Figure S33). This comparison highlights the beneficial impact of the additional $(GOx/TOA\text{-}Au\ NP)_m$ multilayers in promoting faster interfacial electron transfer.

The operational stability of the 5-GOx-5-MTAH anode was further assessed through individual chronoamperometric measurements. After 48 h of continuous operation, the anode retained ~87% of its initial current densities (15.6 mA cm^{-2}) (Figure S34). We also evaluated the long-term operational stability of the 5-GOx-5-MTAH electrode over 20 days and examined the possibility of enzyme leaching during continuous operation. To monitor potential release of GOx, UV–vis spectra of the 10 mmol L^{-1} glucose solution used for daily electrochemical measurements were recorded over 15 days (Figure S35a). No characteristic GOx absorption peak was detected during this period, indicating that enzyme leaching from the 5-GOx-5-MTAH electrode did not occur. In parallel, the electrical conductivity of the electrode was measured daily while subjecting the electrode to fatigue tests involving repeated swelling (wet state) and deswelling (dry state). As shown in Figure S35b, no significant decrease in conductivity was observed over 20 days, confirming that the intrinsic electrical stability of the electrode was well maintained. Despite the absence of enzyme leaching and the preservation of electrical conductivity, long-term electrochemical measurements revealed a gradual decrease in EBFC performance during continuous operation (Figure S35c). This decline is therefore attributed to the inevitable loss of enzymatic activity over extended operation, rather than to electrode degradation or enzyme detachment.

These high anodic current densities and prolonged operational stability are primarily attributed to the synergistic effects of the $(GOx/TOA\text{-}Au\ NP)_m$ multilayer assemblies and the micro-corrugated architecture of the hydrogel-based electrodes, which collectively enhance electron transport efficiency and mechanical robustness.

2.3 | Preparation and Performance of Hydrogel Cathode

The 5-MTAH platform also functions effectively as a cathodic host in EBFCs, where the ORR critically influences both electrochemical efficiency and long-term stability. Enhancing ORR activity is therefore key to improving overall device performance. In this context, embedding Au NPs within the micro-corrugated structure of 5-MTAH provides synergistic benefits. Specifically, the large electroactive surface area and the intrinsic catalytic properties of Au NPs facilitate efficient ORR kinetics, while the

16136829, 2026, 14, Downloaded from https://onlinelibrary.wiley.com/doi/10.1002/smll.202512318 by Kangwon National University, Wiley Online Library on [08/03/2026]. See the Terms and Conditions (https://onlinelibrary.wiley.com/terms-and-conditions) on Wiley Online Library for rules of use; OA articles are governed by the applicable Creative Commons License

corrugated morphology increases the density of accessible active sites, promoting faster reaction rates.

To further boost ORR performance, platinum (Pt)—a benchmark ORR catalyst—was introduced as a co-catalyst. This was achieved by immersing 5-MTAH in a Pt precursor solution followed by chemical reduction using sodium borohydride ($NaBH_4$). The resulting Pt-modified structure (Pt-5-MTAH) exhibited uniform Pt deposition without disrupting the underlying structure (Figure S36).

Based on these results, the ORR performance was evaluated in PBS under nitrogen-saturated, oxygen-saturated, and ambient conditions (Figure S37). At −0.6 V (vs. Ag/AgCl), the areal current densities for Pt-5-MTAH were −17.6 mA cm^{-2} (N_2), −34.0 mA cm^{-2} (ambient), and −53.3 mA cm^{-2} (O_2). When normalized to the N_2 baseline, the cathodic current densities under ambient and O_2 conditions were −16.4 and −35.7 mA cm^{-2}, respectively. In comparison, pristine 5-MTAH (without Pt) exhibited significantly lower current densities under the same conditions: −1.7 mA cm^{-2} (N_2), −3.1 mA cm^{-2} (ambient), and −3.9 mA cm^{-2} (O_2), confirming the superior catalytic activity of Pt-5-MTAH (Figure S38).

The long-term operational stability of Pt-5-MTAH was also assessed under ambient PBS conditions. The Pt-modified electrode retained ~82% of its initial current density after 30 days, whereas pristine 5-MTAH retained only ~71% over the same period (Figure S39). Collectively, these results demonstrate that Pt-5-MTAH achieves substantially enhanced ORR activity, improved charge transfer efficiency, and stable long-term operation, driven by the synergistic combination of highly active Pt catalysts and the robust, electroactive 5-MTAH host electrode.

2.4 | Power Output and Efficiency of Hydrogel-Based EBFCs

To evaluate the practical performance of hydrogel-based EBFCs, the devices were assembled by pairing the 5-GOx-5-MTAH anode with either a Pt-5-MTAH or a pristine 5-MTAH cathode. All tests were conducted in PBS containing 300 or 10 mmol L^{-1} glucose under ambient conditions (Figure 6a). Stationary power output measurements were performed using external resistances ranging from 1 kΩ to 10 MΩ to minimize parasitic currents. In 300 mmol L^{-1} glucose, the complete EBFC (5-GOx-5-MTAH/Pt-5-MTAH) achieved a maximum power density of ~3.7 mW cm^{-2} (corresponding to a volumetric power density of ~112 mW cm^{-3}), approximately 2.3 times higher than the Pt-free device (5-GOx-5-MTAH/5-MTAH), which reached ~1.6 mW cm^{-2} (corresponding to a volumetric power density of ~48 mW cm^{-3}) (Figure 6b; Figure S40a,b). Similarly, in 10 mmol L^{-1} glucose, the complete EBFC delivered ~2.4 mW cm^{-2}, outperforming the Pt-free system (~0.7 mW cm^{-2}) by roughly 3.4-fold (Figure 6c; Figure S40c,d). These results clearly demonstrate the superior power performance of the complete EBFC across both low and high glucose concentrations. This enhancement is attributed to the synergistic pairing of the highly enzyme-active 5-GOx-5-MTAH anode and the Pt-MTAH cathode, whose ORR activity was optimized via $NaBH_4$ reduction. Further supporting this, the complete EBFC exhibited high OCVs of +0.95 V (300 mmol L^{-1}) and +0.92 V (10 mmol L^{-1}), significantly higher than those of the Pt-free system (+0.76 V and +0.62 V, respectively) under ambient conditions.

The hydrogel-based EBFCs also exhibited excellent long-term operational stability. Under ambient conditions with 300 mmol L^{-1} glucose, the complete EBFC retained approximately 2.9 mW cm^{-2} (~78%) of its initial power density after 30 days of continuous operation (Figure 6d). In 10 mmol L^{-1} glucose, it maintained ~1.9 mW cm^{-2} (~80%), while the Pt-free EBFC preserved ~0.5 mW cm^{-2} (~77%) over the same period. Voltage retention measurements showed similar trends (Figure 6e): the complete EBFC maintained ~84% (+0.80 V) and ~86% (+0.79 V) of its initial OCVs in 300 and 10 mmol L^{-1} glucose, respectively, whereas the Pt-free EBFC retained ~81% (+0.62 V) and ~85% (+0.53 V) under the same conditions. During the 30-day stability test, the electrolyte reservoir (50 mL) was periodically replenished with glucose to maintain each constant concentration, 10 and 300 mmol L^{-1}. This controlled-fuel condition ensured that the EBFCs operated without significant substrate depletion, allowing the observed performance decay to primarily reflect the intrinsic long-term stability of the immobilized enzymes rather than glucose exhaustion. The gradual decrease is attributed to the natural denaturation of GOx during extended operation, consistent with previously reported EBFC aging behavior [70]. This remarkable stability is primarily attributed to the hierarchical electrode design, incorporating multiple interfacial and structural strategies: (i) capillary force- and ligand exchange-driven integration of metal NPs between PEI and TOA-Au NPs, (ii) covalent bonding between TREN and TOA-Au NPs, and (iii) amphiphilic co-assembly of GOx and TOA-Au NPs.

3 | Conclusion

In this study, we demonstrated the development of hydrogel-based EBFCs that possess highly flexible and biocompatible properties, high electron transfer efficiency, elevated areal power density, and long-term operational stability. These characteristics were achieved through capillary force and ligand exchange-induced metal NPs assemblies. Notably, the infiltrated PEI within hydrogel acts as both a cross-linker to control the mechanical properties of hydrogel and a strong binding linker between hydrogel and Au NPs, as well as a transforming additive for the formation of Au nanoplates. This process yielded a highly conductive 5-MTAH with exceptional electrical conductivity of ~1.5×10^5 S cm^{-1} and micro-corrugated surface morphology via adsorption during repetitive swelling/deswelling cycles, which maintains highly stable electrical properties under various mechanical stresses. When additional $(GOx/TOA\text{-}Au\ NP)_m$ multilayers were LbL-assembled on the 5-MTAH as an anode and a Pt-5-MTAH served as a cathode, the resulting hydrogel-based EBFC exhibited an exceptional power output of ~3.7 mW cm^{-2} and retained ~80% efficiency of its initial areal power density even after 30 days of continuous operation. Considering that our strategy is based on interfacial assembly to enhance both electron transfer kinetics and enzyme immobilization, it offers broad potential for hydrogel-based electrodes not only in EBFCs but also in various electrochemical systems that demand high surface area, mechanical durability, and long-term operational stability.

16136829, 2026, 14, Downloaded from https://onlinelibrary.wiley.com/doi/10.1002/smll.202512318 by Kangwon National University, Wiley Online Library on [08/03/2026]. See the Terms and Conditions (https://onlinelibrary.wiley.com/terms-and-conditions) on Wiley Online Library for rules of use; OA articles are governed by the applicable Creative Commons License

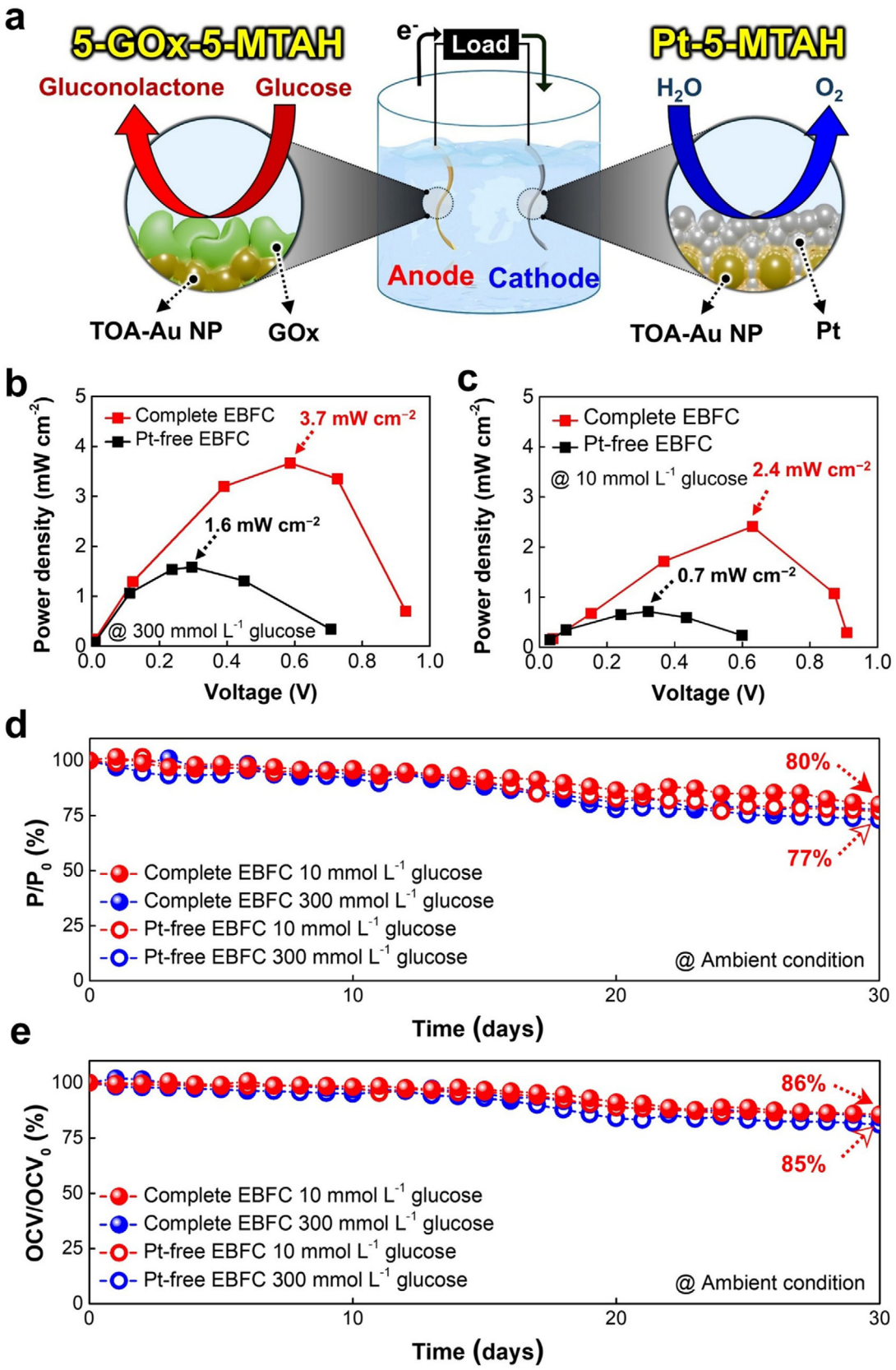

FIGURE 6 | Performance of the hydrogel-based EBFCs. (a) Schematic illustration of the EBFC system. (b) Power output of the hydrogel-based EBFCs in PBS solutions containing 300 mmol L^{-1} glucose at 36.5°C. (c) Power output of the hydrogel-based EBFCs in PBS solutions containing 10 mmol L^{-1} glucose at 36.5°C. (d) Relative power retention (P/P_0) of the hydrogel-based EBFCs in PBS solutions containing 300 mmol L^{-1} and 10 mmol L^{-1} glucose at 36.5°C. (e) Relative OCV retention (OCV/OCV_0) of the hydrogel-based EBFCs in PBS solutions containing 300 mmol L^{-1} glucose and 10 mmol L^{-1} glucose at 36.5°C.

16136829, 2026, 14, Downloaded from https://onlinelibrary.wiley.com/doi/10.1002/smll.202512318 by Kangwon National University, Wiley Online Library on [08/03/2026]. See the Terms and Conditions (https://onlinelibrary.wiley.com/terms-and-conditions) on Wiley Online Library for rules of use; OA articles are governed by the applicable Creative Commons License

4 | Experimental Section

The detailed experimental information is available in the part of the Supporting Information.

Acknowledgements

This work was supported by the National Research Foundation of Korea (NRF) funded by the Ministry of Science and ICT of Korean government (NRF-2022R1A2C1009690, RS-2025-02214734, and RS-2024-00352893) and Ministry of Education (RS-2025-25433905). It was also supported by the Regional Innovation System & Education (RISE) Program through the Gangwon RISE Center, funded by the Ministry of Education (MOE) and the Gangwon State, Republic of Korea (2025-RISE-10-002).

Conflicts of Interest

The authors declare no conflict of interest.

Data Availability Statement

The data that support the findings of this study are available from the corresponding author upon reasonable request.

References

1. S. Calabrese Barton, J. Gallaway, and P. Atanassov, "Enzymatic Biofuel Cells for Implantable and Microscale Devices," *Chemical Reviews* 104 (2004): 4867–4886.

2. H. Liu, S. S. You, Z. Gao, N. Hu, and Y. Zhao, "Next Generation of Gastrointestinal Electrophysiology Devices," *Nature Reviews Gastroenterology & Hepatology* 21 (2024): 457–458.

3. J. Pak, W. Chang, C. H. Kwon, and J. Cho, "Recent Advances in Enzyme-Based Biofuel Cells Using Glucose Fuel: Achieving High Power Output and Enhanced Operational Stability," *Advanced Functional Materials* 35 (2025): 2415933.

4. Z. Gao, Y. Zhou, Z. Foroughi, et al., "Advanced Energy Harvesters and Energy Storage for Powering Wearable and Implantable Medical Devices," *Advanced Materials* 36 (2024): 2404492.

5. M. Kang, D. Nam, J. Ahn, et al., "A Mediator-Free Multi-Ply Biofuel Cell Using an Interfacial Assembly Between Hydrophilic Enzymes and Hydrophobic Conductive Oxide Nanoparticles With Pointed Apexes," *Advanced Materials* 35 (2023): 2304986.

6. S.-Y. Yang, V. Sencadas, S. S. You, et al., "Powering Implantable and Ingestible Electronics," *Advanced Functional Materials* 31 (2021): 2009289.

7. D. Lee, S. H. Jeong, S. Yun, et al., "Totally Implantable Enzymatic Biofuel Cell and Brain Stimulator Operating in Bird Through Wireless Communication," *Biosensors and Bioelectronics* 171 (2021): 112746.

8. A. Niiyama, K. Murata, Y. Shigemori, A. Zebda, and S. Tsujimura, "High-Performance Enzymatic Biofuel Cell Based on Flexible Carbon Cloth Modified with Mgo-Templated Porous Carbon," *Journal of Power Sources* 427 (2019): 49–55.

9. C. H. Kwon, M. Kang, M. Kwon, et al., "High-Performance Hybrid Biofuel Cells Using Amphiphilic Assembly Based Enzyme Electrodes," *Applied Physics Reviews* 9 (2022): 021413.

10. X. Xiao, K. D. McGourty, and E. Magner, "Enzymatic Biofuel Cells for Self-Powered, Controlled Drug Release," *Journal of the American Chemical Society* 142 (2020): 11602–11609.

11. X. Xiao, H. Xia, R. Wu, et al., "Tackling the Challenges of Enzymatic (Bio)Fuel Cells," *Chemical Reviews* 119 (2019): 9509–9558.

12. H. Wu, Y. Zhang, A. L. Kjøniksen, X. Zhou, and X. Zhou, "Wearable Biofuel Cells: Advances From Fabrication to Application," *Advanced Functional Materials* 31 (2021): 2103976.

13. M. S. Rahman, A. Shon, R. Joseph, et al., "Soft, Stretchable Conductive Hydrogels for High-Performance Electronic Implants," *Science Advances* 11 (2025): ads4415.

14. S. Odinotski, K. Dhingra, A. GhavamiNejad, et al., "A Conductive Hydrogel-Based Microneedle Platform for Real-Time pH Measurement in Live Animals," *Small* 18 (2022): 2200201.

15. J. Zhang, S. Shen, R. Lin, et al., "Highly Stretchable and Biocompatible Wrinkled Nanoclay-Composite Hydrogel With Enhanced Sensing Capability for Precise Detection of Myocardial Infarction," *Advanced Materials* 35 (2023): 2209497.

16. C. H. Kwon, S.-H. Lee, Y.-B. Choi, et al., "High-Power Biofuel Cell Textiles From Woven Biscrolled Carbon Nanotube Yarns," *Nature Communications* 5 (2014): 3928.

17. H. Sakai, T. Nakagawa, Y. Tokita, et al., "A High-Power Glucose/Oxygen Biofuel Cell Operating Under Quiescent Conditions," *Energy & Environmental Science* 2 (2009): 133–138.

18. Z. Kang, K. Jiao, J. Cheng, R. Peng, S. Jiao, and Z. Hu, "A Novel Three-Dimensional Carbonized PANI1600@Cnts Network For Enhanced Enzymatic Biofuel Cell," *Biosensors and Bioelectronics* 101 (2018): 60–65.

19. Y. Sun, T. Qin, X. Liu, Y. Liu, D. Zhao, and D. K. Wong, "A High-Performance Hybrid Biofuel Cell with a Honeycomb-Like Ti 3 C 2 T x /MWCNT/AuNP Bioanode and a ZnCo 2 @NCNT Cathode for Self-Powered Biosensing," *Small* 19 (2023): 2206257.

20. Z. Kang, Y.-H. P. J. Zhang, and Z. Zhu, "A Shriveled Rectangular Carbon Tube with the Concave Surface For High-Performance Enzymatic Glucose/O2 Biofuel Cells," *Biosensors and Bioelectronics* 132 (2019): 76–83.

21. N. Mano, "Engineering Glucose Oxidase for Bioelectrochemical Applications," *Bioelectrochemistry* 128 (2019): 218–240.

22. X. Huang, H. Li, J. Li, et al., "Transient, Implantable, Ultrathin Biofuel Cells Enabled by Laser-Induced Graphene and Gold Nanoparticles Composite," *Nano Letters* 22 (2022): 3447–3456.

23. Y. Song and C. Wang, "High-Power Biofuel Cells Based on Three-Dimensional Reduced Graphene Oxide/Carbon Nanotube Micro-Arrays," *Microsystems & Nanoengineering* 5 (2019): 46.

24. Y. Chen, P. Gai, J. Zhang, and J.-J. Zhu, "Design of an Enzymatic Biofuel Cell with Large Power Output," *Journal of Materials Chemistry A* 3 (2015): 11511–11516.

25. A. Zebda, C. Gondran, A. L. Goff, M. Holzinger, P. Cinquin, and S. Cosnier, "Mediatorless High-Power Glucose Biofuel Cells Based on Compressed Carbon Nanotube-Enzyme Electrodes," *Nature Communications* 2 (2011): 370.

26. A. Trifonov, A. Stemmer, and R. Tel-Vered, "Power Generation by Selective Self-Assembly of Biocatalysts," *ACS Nano* 13 (2019): 8630–8638.

27. Y. Chung, D. C. Tannia, and Y. Kwon, "Glucose Biofuel Cells Using Bi-Enzyme Catalysts Including Glucose Oxidase, Horseradish Peroxidase and Terephthalaldehyde Crosslinker," *Chemical Engineering Journal* 334 (2018): 1085–1092.

28. Y. Chung, Y. Ahn, M. Christwardana, H. Kim, and Y. Kwon, "Development of a Glucose Oxidase-Based Biocatalyst Adopting Both Physical Entrapment and Crosslinking, and Its Use in Biofuel Cells," *Nanoscale* 8 (2016): 9201–9210.

29. T. Xue, B. Peng, M. Xue, et al., "Integration of Molecular and Enzymatic Catalysts on Graphene For Biomimetic Generation of Antithrombotic Species," *Nature Communications* 5 (2014): 3200.

30. M. Sun, P. Li, H. Qin, et al., "Liquid Metal/Cnts Hydrogel-Based Transparent Strain Sensor For Wireless Health Monitoring of Aquatic Animals," *Chemical Engineering Journal* 454 (2023): 140459.

31. Y. Chen, D. Estevez, Z. Zhu, Y. Wang, Y.-W. Mai, and F. Qin, "Multifunctional Conductive Hydrogel Composites With Nickel Nanowires and

16136829, 2026, 14, Downloaded from https://onlinelibrary.wiley.com/doi/10.1002/smll.202512318 by Kangwon National University, Wiley Online Library on [08/03/2026]. See the Terms and Conditions (https://onlinelibrary.wiley.com/terms-and-conditions) on Wiley Online Library for rules of use; OA articles are governed by the applicable Creative Commons License

Liquid Metal Conductive Highways," *ACS Applied Materials & Interfaces* 16 (2024): 29267–29281.

32. C. Lim, S. Lee, H. Kang, et al., "Highly Conductive and Stretchable Hydrogel Nanocomposite Using Whiskered Gold Nanosheets for Soft Bioelectronics," *Advanced Materials* 36 (2024): 2407931.

33. Y. Ohm, C. Pan, M. J. Ford, X. Huang, J. Liao, and C. Majidi, "An Electrically Conductive Silver–Polyacrylamide–Alginate Hydrogel Composite For Soft Electronics," *Nature Electronics* 4 (2021): 185–192.

34. Y. Zhao, Y. Ohm, J. Liao, et al., "A Self-Healing Electrically Conductive Organogel Composite," *Nature Electronics* 6 (2023): 206–215.

35. Q. Zhou, J. Lyu, G. Wang, et al., "Mechanically Strong and Multifunctional Hybrid Hydrogels With Ultrahigh Electrical Conductivity," *Advanced Functional Materials* 31 (2021): 2104536.

36. C. Chen, X. Pang, Y. Li, and X. Yu, "Ultrafast Self-Healing, Super-stretchable, and Ultra-Strong Polymer Cluster-Based Adhesive Based on Aromatic Acid Cross-Linkers for Excellent Hydrogel Strain Sensors," *Small* 20 (2024): 2305875.

37. J. Chong, C. Sung, K. S. Nam, et al., "Highly Conductive Tissue-Like Hydrogel Interface Through Template-Directed Assembly," *Nature Communications* 14 (2023): 2206.

38. P. Rahmani, A. Shojaei, and M. D. Dickey, "A Highly Conductive and Ultra-Stretchable Polyaniline/Cellulose Nanocrystal/Polyacrylamide Hydrogel With Hydrophobic Associations For Wearable Strain Sensors," *Journal of Materials Chemistry A* 12 (2024): 9552–9562.

39. Y. Shin, H. S. Lee, Y. J. Hong, et al., "Low-Impedance Tissue-Device Interface Using Homogeneously Conductive Hydrogels Chemically Bonded To Stretchable Bioelectronics," *Science Advances* 10 (2024): adi7724.

40. T. Zhou, H. Yuk, F. Hu, et al., "3D Printable High-Performance Conducting Polymer Hydrogel For All-Hydrogel Bioelectronic Interfaces," *Nature Materials* 22 (2023): 895–902.

41. Q. He, Y. Cheng, Y. Deng, F. Wen, Y. Lai, and H. Li, "Conductive Hydrogel for Flexible Bioelectronic Device: Current Progress and Future Perspective," *Advanced Functional Materials* 34 (2024): 2308974.

42. X. P. Hao, C. Y. Li, C. W. Zhang, et al., "Self-Shaping Soft Electronics Based on Patterned Hydrogel With Stencil-Printed Liquid Metal," *Advanced Functional Materials* 31 (2021): 2105481.

43. M. Kotal, J. Kim, R. Tabassian, et al., "Highly Bendable Ionic Soft Actuator Based on Nitrogen-Enriched 3D Hetero-Nanostructure Electrode," *Advanced Functional Materials* 28 (2018): 1802464.

44. H. S. Wang, J. Cho, D. S. Song, J. H. Jang, J. Y. Jho, and J. H. Park, "High-Performance Electroactive Polymer Actuators Based on Ultrathick Ionic Polymer–Metal Composites With Nanodispersed Metal Electrodes," *ACS Applied Materials & Interfaces* 9 (2017): 21998–22005.

45. Y. Yan, T. Santaniello, L. G. Bettini, et al., "Electroactive Ionic Soft Actuators with Monolithically Integrated Gold Nanocomposite Electrodes," *Advanced Materials* 29 (2017): 1606109.

46. L. Zhong, L. Tang, S. Yang, Z. Zhao, Z. Zheng, and X. Jiang, "Stretchable Liquid Metal-Based Metal-Polymer Conductors for Fully Screen-Printed Biofuel Cells," *Analytical Chemistry* 94 (2022): 16738–16745.

47. A. J. Bandodkar, I. Jeerapan, J.-M. You, R. Nuñez-Flores, and J. Wang, "Highly Stretchable Fully-Printed CNT-Based Electrochemical Sensors and Biofuel Cells: Combining Intrinsic and Design-Induced Stretchability," *Nano Letters* 16 (2016): 721–727.

48. Y. Chen, X. Wan, G. Li, J. Ye, J. Gao, and D. Wen, "Metal Hydrogel-Based Integrated Wearable Biofuel Cell for Self-Powered Epidermal Sweat Biomarker Monitoring," *Advanced Functional Materials* 34 (2024): 2404329.

49. S. Guan, J. Wang, Y. Yang, et al., "Highly Stretchable and Flexible Electrospinning-Based Biofuel Cell for Implantable Electronic," *Advanced Functional Materials* 33 (2023): 2303134.

50. Y. Yuan, Z. Zhang, J. Cao, X. Zhao, L. Ye, and G. Wang, "Self-Adhesive Wearable Poly (Vinyl Alcohol)-Based Hybrid Biofuel Cell Powered By Human Bio-Fluids," *Biosensors and Bioelectronics* 247 (2024): 115930.

51. Z. Han, P. Wang, Y. Lu, Z. Jia, S. Qu, and W. Yang, "A Versatile Hydrogel Network–Repairing Strategy Achieved By The Covalent-Like Hydrogen Bond Interaction," *Science Advances* 8 (2022): abl5066.

52. C. Keplinger, J.-Y. Sun, C. C. Foo, P. Rothemund, G. M. Whitesides, and Z. Suo, "Stretchable, Transparent, Ionic Conductors," *Science* 341 (2013): 984–987.

53. B. Wang, F. Dong, X. Sun, et al., "Biphase Ionic Hydrogels With Ultrasoftness and High Conductivity for Bio-Ionotronics," *ACS Nano* 19 (2025): 16488–16499.

54. S. Wang, L. Yu, S. Wang, et al., "Strong, Tough, Ionic Conductive, and Freezing-Tolerant All-Natural Hydrogel Enabled by Cellulose-Bentonite Coordination Interactions," *Nature Communications* 13 (2022): 3408.

55. J. Ko, D. Kim, Y. Song, et al., "Electroosmosis-Driven Hydrogel Actuators Using Hydrophobic/Hydrophilic Layer-By-Layer Assembly-Induced Crack Electrodes," *ACS Nano* 14 (2020): 11906–11918.

56. J. N. Israelachvili, *Intermolecular and Surface Forces* (Academic Press, 2011).

57. S. Kang, D. Nam, J. Choi, et al., "Highly Conductive Paper/Textile Electrodes Using Ligand Exchange Reaction-Induced in Situ Metallic Fusion," *ACS Applied Materials & Interfaces* 11 (2019): 12032–12042.

58. Y. Ko, M. Kwon, W. K. Bae, B. Lee, S. W. Lee, and J. Cho, "Flexible Supercapacitor Electrodes Based on Real Metal-Like Cellulose Papers," *Nat Communications* 8 (2017): 536.

59. B. A. Korgel, S. Fullam, S. Connolly, and D. Fitzmaurice, "Assembly and Self-Organization of Silver Nanocrystal Superlattices: Ordered "Soft Spheres"," *The Journal of Physical Chemistry B* 102 (1998): 8379–8388.

60. Y. Kim, J. Zhu, B. Yeom, et al., "Stretchable Nanoparticle Conductors with Self-Organized Conductive Pathways," *Nature* 500 (2013): 59–63.

61. T. Udayabhaskararao, T. Altantzis, L. Houben, et al., "Tunable Porous Nanoallotropes Prepared by Post-Assembly Etching of Binary Nanoparticle Superlattices," *Science* 358 (2017): 514–518.

62. C. Xing, S. Zhong, D. Liu, et al., "Hydrogel Film@Au Nanoparticle Arrays Based on Self-Assembly Co-Assisted by Electrostatic Attraction and Hydrogel-Shrinkage for SERS Detection With Active Gaps," *Advanced Materials Interfaces* 8 (2021): 2101055.

63. J. Schmitt, G. Decher, W. J. Dressick, et al., "Metal Nanoparticle/Polymer Superlattice Films: Fabrication and Control of Layer Structure," *Advanced Materials* 9 (1997): 61–65.

64. R. A. Blaik, E. Lan, Y. Huang, and B. Dunn, "Gold-Coated M13 Bacteriophage as a Template for Glucose Oxidase Biofuel Cells With Direct Electron Transfer," *ACS Nano* 10 (2016): 324–332.

65. E. Laviron, "General Expression of the Linear Potential Sweep Voltammogram in the Case of Diffusionless Electrochemical Systems," *Journal of Electroanalytical Chemistry and Interfacial Electrochemistry* 101 (1979): 19–28.

66. M. H. Kabir, E. Marquez, G. Djokoto, et al., "Energy Harvesting by Mesoporous Reduced Graphene Oxide Enhanced the Mediator-Free Glucose-Powered Enzymatic Biofuel Cell for Biomedical Applications," *ACS Applied Materials & Interfaces* 14 (2022): 24229–24244.

67. J. Huang, Y. Zhang, X. Deng, et al., "Self-Encapsulated Enzyme Through In-Situ Growth of Polypyrrole For High-Performance Enzymatic Biofuel Cell," *Chemical Engineering Journal* 429 (2022): 132148.

68. J. Liu, K. Liu, X. Liu, X. Zhu, X. Liu, and S. Alwarappan, "Self-Powered Biosensor Driven by a Hybrid Biofuel Cell with CuCoP-Polyoxometallate Composite as Both Cathode Catalyst and Sensing Interface," *Small* 21 (2025): 2500451.

69. N. S. Ridhuan, K. A. Razak, and Z. Lockman, "Fabrication and Characterization of Glucose Biosensors by Using Hydrothermally Grown ZnO Nanorods," *Scientific Reports* 8 (2018): 13722.

16136829, 2026, 14, Downloaded from https://onlinelibrary.wiley.com/doi/10.1002/smll.202512318 by Kangwon National University, Wiley Online Library on [08/03/2026]. See the Terms and Conditions (https://onlinelibrary.wiley.com/terms-and-conditions) on Wiley Online Library for rules of use; OA articles are governed by the applicable Creative Commons License

70. C. H. Kwon, Y. Ko, D. Shin, S. W. Lee, and J. Cho, "Highly Conductive Electrocatalytic Gold Nanoparticle-Assembled Carbon Fiber Electrode For High-Performance Glucose-Based Biofuel Cells," *Journal of Materials Chemistry A* 7 (2019): 13495–13505.

Supporting Information

Additional supporting information can be found online in the Supporting Information section.

Supporting File: smll72092-sup-0001-SuppMat.docx

Supporting File: smll72092-sup-0002-Movie S1.mp4

16136829, 2026, 14, Downloaded from https://onlinelibrary.wiley.com/doi/10.1002/smll.202512318 by Kangwon National University, Wiley Online Library on [08/03/2026]. See the Terms and Conditions (https://onlinelibrary.wiley.com/terms-and-conditions) on Wiley Online Library for rules of use; OA articles are governed by the applicable Creative Commons License